



HAL
open science

Mars ultraviolet dayglow variability: SPICAM observations and comparison with airglow model

Christopher M. Cox, J.-C. Gérard, B. Hubert, Jean-Loup Bertaux, S. W. Bougher

► **To cite this version:**

Christopher M. Cox, J.-C. Gérard, B. Hubert, Jean-Loup Bertaux, S. W. Bougher. Mars ultraviolet dayglow variability: SPICAM observations and comparison with airglow model. *Journal of Geophysical Research. Planets*, 2010, 115 (E4), pp.E04010. 10.1029/2009JE003504 . hal-00477772

HAL Id: hal-00477772

<https://hal.science/hal-00477772>

Submitted on 16 Jul 2020

HAL is a multi-disciplinary open access archive for the deposit and dissemination of scientific research documents, whether they are published or not. The documents may come from teaching and research institutions in France or abroad, or from public or private research centers.

L'archive ouverte pluridisciplinaire **HAL**, est destinée au dépôt et à la diffusion de documents scientifiques de niveau recherche, publiés ou non, émanant des établissements d'enseignement et de recherche français ou étrangers, des laboratoires publics ou privés.



Mars ultraviolet dayglow variability: SPICAM observations and comparison with airglow model

C. Cox,¹ J.-C. Gérard,¹ B. Hubert,¹ J.-L. Bertaux,² and S. W. Bougher³

Received 8 September 2009; revised 13 November 2009; accepted 11 December 2009; published 30 April 2010.

[1] Dayglow ultraviolet emissions of the CO Cameron bands and the CO₂⁺ doublet in the Martian atmosphere have been observed with the Spectroscopy for Investigation of Characteristics of the Atmosphere of Mars on board the Mars Express spacecraft. A large amount of limb profiles has been obtained which makes it possible to analyze variability of the brightness as well as of the altitude of the emission peak. Focusing on one specific season (Ls = [90,180] °), we find that the average CO peak brightness is equal to 118 ± 33 kR, with an average peak altitude of 121.1 ± 6.5 km. Similarly, the CO₂⁺ emission shows a mean brightness of 21.6 ± 7.2 kR with a peak located at 119.1 ± 7.0 km. We show that the brightness intensity of the airglows is mainly controlled by the solar zenith angle and by solar activity. Moreover, during Martian summer of year 2005, an increase of the airglow peak altitude has been observed between Ls = 120° and 180°. We demonstrate that this variation is due to a change in the thermospheric local CO₂ density, in agreement with observations performed by stellar occultation. Using a Monte Carlo one-dimensional model, we also show that the main features of the emission profiles can be reproduced for the considered set of data. However, we find it necessary to scale the calculated intensities by a fixed factor.

Citation: Cox, C., J.-C. Gérard, B. Hubert, J.-L. Bertaux, and S. W. Bougher (2010), Mars ultraviolet dayglow variability: SPICAM observations and comparison with airglow model, *J. Geophys. Res.*, 115, E04010, doi:10.1029/2009JE003504.

1. Introduction

[2] Cameron CO band system and CO₂⁺ doublet emissions are well known features of the Mars dayside airglow. They were first observed by *Barth et al.* [1971] during the Mariner 6 mission and have been studied so far with different instruments, on board various spacecraft. A list of previous observations is given in Table 1. As shown in Figure 1, the CO Cameron bands range from 170 nm to 270 nm and correspond to forbidden transitions of CO molecules excited in the (a³Π) state to the ground state. Processes believed to contribute to the production of CO (a³Π) molecules are listed in Table 2. The CO₂⁺ doublet emission is observed at 298 nm and 299 nm and corresponds to the CO₂⁺ (B²Σ⁺ → X²Σ⁺) transition. It is produced by mechanisms presented in Table 3 with their corresponding references. The molecules in the excited state deexcite to the ground state while emitting photons in the ultraviolet wavelength domain. From the processes listed in Tables 2 and 3 and results of earlier studies, it follows that these emissions are mainly con-

trolled by the CO₂ density and by photoelectrons as well as solar photon flux impacting the upper atmosphere of Mars. Once the emissions processes are identified, the study of these emissions can provide useful information about the Martian major constituent, namely CO₂. This can be quantified using models that calculate the various sources of excitation, depending on several input quantities such as solar zenith angle, solar longitude, latitude and solar activity.

[3] Observations used in this study have been performed with the Spectroscopy for Investigation of Characteristics of the Atmosphere of Mars (SPICAM) instrument, on board the Mars Express (MEX) spacecraft. SPICAM is composed of an ultraviolet and an infrared spectrometer. Its ultraviolet domain ranges from 118 nm to 320 nm which includes many spectral features of the Mars dayglow as illustrated in Figure 1, such as the CO (a³Π – X¹Σ⁺) Cameron bands, the CO₂⁺ (B²Σ⁺ – X²Π) doublet, the OI 130.6 nm triplet, the OI 135.6 nm doublet and OI 297.2 nm, the CO (A¹Π – X¹Σ⁺) fourth positive bands, the 156.1 nm and 165.7 nm CI multiplets, the H I 121.6 nm Lyman-α emission, the NI 120.0 nm emission and the CO⁺ (B²Σ⁺ – X²Σ⁺) transition [*Barth et al.*, 1971; *Anderson and Hord*, 1971; *Stewart et al.*, 1972; *Strickland et al.*, 1972, 1973; *Gutcheck and Zipf*, 1973; *Fox and Dalgarno*, 1979; *Conway*, 1981; *Feldman et al.*, 2000; *Leblanc et al.*, 2006].

[4] Some of these emissions can hardly be quantitatively analyzed using SPICAM observations because their signal-to-noise ratio is too low. However, the CO Cameron and the

¹Laboratoire de Physique Atmosphérique et Planétaire, Université de Liège, Liège, Belgium.

²LATMOS, Guyancourt, France.

³Department of Atmospheric, Oceanic and Space Sciences, University of Michigan, Ann Arbor, Michigan, USA.

Table 1. Observations of the Martian UV Dayglow

| Mission | Year ^a | Instrument | Observations | References |
|-----------------|-------------------|------------|---------------------------|---|
| Mariner 6 and 7 | 1969 | UVS | Mars orbiting spacecraft | <i>Barth et al.</i> [1971], <i>Stewart</i> [1972], <i>Strickland et al.</i> [1972] |
| Mariner 9 | 1971 | UVS | Mars orbiting spacecraft | <i>Stewart et al.</i> [1972], <i>Strickland et al.</i> [1973], <i>Barth et al.</i> [1972] |
| Astro-2 | 1995 | HUT | Earth orbiting spacecraft | <i>Feldman et al.</i> [2000] |
| Mars Express | 2003 | SPICAM | Mars orbiting spacecraft | <i>Leblanc et al.</i> [2006] |

^aThe year is the date when scientific data began to be collected.

CO₂⁺ doublet emissions may be investigated in detail and compared with model calculations.

2. Observations

[5] SPICAM dayglow observations extend over several Martian seasons and a wide range of solar zenith angles. The spacecraft follows a nearly polar eccentric orbit of 6.72 h period with pericenter and apocenter located at 298 km and 10,107 km, respectively. The orbital plane precesses and leads to different pointing configurations. Dayglow observations are performed in the tangential “grazing” limb mode where the line of sight crosses the atmosphere twice [*Bertaux et al.*, 2006]. This mode allows one to maximize the time of observation of the atmosphere, which is typically 20 min and is appropriate to avoid solar reflection on the limb haze. Each second, five spectra are recorded by the instrument, corresponding to five adjacent parts of the CCD called “spatial bins.” The integration period is of 640 ms and the remaining time is used to average the spectra of each part of the CCD and to read out the signal. The position and size of each read part of the CCD are fixed by preselected parameters called “bin” and “first read line.” The bin parameter determines the number of spectra averaged in each part of the CCD and the first read line controls the beginning of the overall read portion. Depending on these two parameters, the signal is either diffracted through a small (50 μm) or a large (500 μm) slit, providing spectral resolutions of 1.5 nm and 6 nm, respectively. Five different but close altitudes, latitudes, local times and thus, solar zenith angles, are observed at the tangent point along the line of sight, corresponding to each spatial bin. The combination of the bin parameter (ranging from 2 to 32), the pixel field of view of 0.7 arc min and the distance from the spacecraft to the tangent point leads to a vertical spatial resolution of a few kilometers or less.

[6] Since the beginning of the mission, hundreds of dayglow observations have been performed. However, a part of these data is not usable for quantitative analysis. This limitation is caused by several factors. First, the line of sight sometimes crosses the limb at altitudes where solar photons are reflected by the haze, leading to the CCD saturation; second, from Medium Term Plan (MTP) 23 (13 February 2006), onward, an anomalous high-frequency signal randomly appears. Finally, stray light sometimes appears as a broad peak centered at 250 nm [*Bertaux et al.*, 2006, Figure 17] and is due to solar light scattering inside the instrument. After all the database had been sorted, we have selected a total of 46 orbits presenting suitable dayglow observations. Selected observations are then processed by removing the dark current component, and subtracting offset and background signal. These steps are performed using technological observations obtained with a null signal am-

plification and using exactly the same observation parameters (bin, first read line, integration time). The absolute calibration is then performed using well-known hot star spectra, following the formula presented by *Cox et al.* [2008].

[7] For this analysis, we have chosen to use only data collected with the small slit to get sufficient spectral resolution and because the large slit sometimes presents saturated signals or excessive stray light. The spatial bins are then summed to form one single observation per orbit, therefore presenting two limb profiles (one for egress, one for ingress) as was illustrated by *Gérard et al.* [2008a, Figure 1] in the case of SPICAV observations for Venus Express. We have then integrated each spectrum over their respective wavelength domain. As was discussed by *Simon et al.* [2009], the spectral interval of the Cameron bands also contains weaker CO fourth positive bands (A¹Π–X¹Σ⁺). Direct integration over the range of Cameron band emission range leads to observed intensities overestimated by ≈15%. Therefore, our calculated intensities for the Cameron bands are obtained by correcting the integrated intensity in this domain for this additional contribution. Thus, the CO Cameron brightness refers to the integrated band brightness, corrected for underlying emissions.

[8] As it is illustrated in Figure 2, in order to limit the effect of seasonal variations, we also restricted our study to the analysis of one specific season determined by solar longitudes ranging from 90° to 180° and included in Mars year 27 dust season (see *McDunn et al.* [2010, Figure 2] for more details). Therefore, this selection reduces our data set to 33 orbits instead of the 46 initial ones. Finally N = 66 limb profiles have been analyzed (one egress and one ingress per

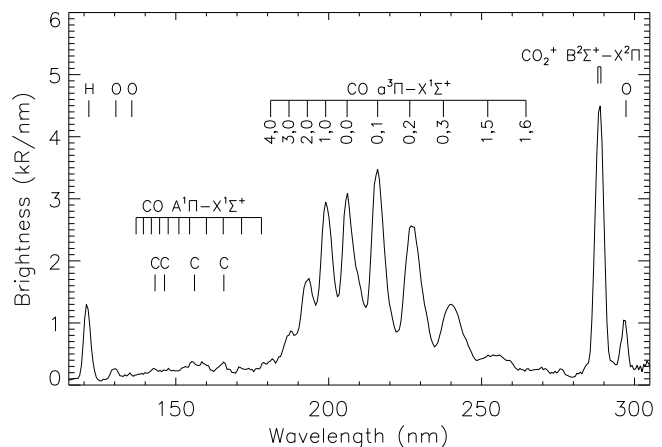


Figure 1. Spectrum of the Mars ultraviolet dayglow. It has been obtained by averaging all spectra recorded by SPICAM during orbit 1267 while the line of sight was crossing altitudes between 100 and 150 km.

Table 2. CO* Production Processes for CO Cameron Bands and References for Cross Sections and Rate Coefficients^a

| Process | Reactions | References |
|----------------|--|---|
| 1 | $\text{CO} + e^- \rightarrow \text{CO}^* + e^-$ | <i>Shirai et al.</i> [2001] |
| 2 | $\text{CO}_2 + e^- \rightarrow \text{CO}^* + \text{O}^* + e^-$ | <i>Shirai et al.</i> [2001] |
| 3 ^b | $\text{CO}_2 + h\nu \rightarrow \text{CO}^* + \text{O}^*$ | <i>Lawrence</i> [1972] |
| 4 ^c | $\text{CO}_2^+ + e^- \rightarrow \text{CO}^* + \text{O}$ | <i>Fox</i> [2004], <i>Hanson et al.</i> [1977], <i>Seiersen et al.</i> [2003], <i>Skrzypkowski et al.</i> [1998], <i>Rosati et al.</i> [2003] |

^aThe photoionization and photoabsorption cross-section data and branching ratios for CO₂, CO, O, and N₂ were taken from the Photo Cross Sections and Rate Coefficients database by W. Huebner and R. Link (<http://amop.space.swri.edu/>) [*Huebner et al.*, 1992].

^bThe cross section for this process was calculated as the total CO₂ photoabsorption cross section multiplied by the branching ratio taken from *Lawrence* [1972].

^cTo evaluate the contribution of CO₂⁺ dissociative recombination as a source of CO Cameron bands, we use the results from *Fox's* [2004] study where densities of CO₂⁺ and electrons were calculated for low solar activity. The electron temperature was taken from *Hanson et al.* [1977], the rate coefficient was taken from *Seiersen et al.* [2003], and the branching ratios of dissociative recombination of CO₂⁺ to the state a³Σ were adopted from *Skrzypkowski et al.* [1998] and *Rosati et al.* [2003].

orbit). To obtain smooth limb profiles, we have applied a spatial low-pass filter to remove the statistical noise from the observations and to better determine the peak altitudes and brightness intensities. A typical limb profile extracted from orbit 1267 (12 January 2005) is shown in Figure 3, where we also plotted the raw profile in 5 km altitude bins. It shows both the CO Cameron and the CO₂⁺ profiles, which present peak intensities of 115.2 kR and 19.7 kR at altitudes of 125.5 km and 124.5 km, respectively. Adopting the same methodology for the selected orbits, we constructed histogram distributions of peak altitudes and brightness for both CO Cameron and CO₂⁺ doublet emissions. These plots are presented in Figures 4a, 4c, 4e, and 4g. The comparison with modeled profiles will be discussed later. The characteristics of the distributions are given in Table 4 where one notes that the average peak altitudes of CO₂⁺ and CO Cameron are very close, with the Cameron emission peak statistically located 2.0 km above the CO₂⁺ doublet airglow. The standard deviations of the altitudes proposed in Table 4 only reflect the actual variability of the emission altitude since their values are much larger than the pointing accuracy of the instrument. The gap between the two layers is therefore significant since it has been determined from each observation and has a standard deviation of 1.3 km, indicating that the two airglow layers move together in the atmosphere. The brightness of the CO Cameron emission is about five times higher than the CO₂⁺ emission. We also note that the distributions are widespread over a large range of values, with standard deviations as large as 28% for CO Cameron peak brightness, which includes the 1/N^{1/2} statistical error. This variability reflects the way into which different physical processes come into play to control the emissions intensities and their peak altitudes. In order to find the different contributions of each of them, we now present Figures 5, 6, 7, 8, and 9, which explain the details of the different mechanisms that can modify the brightness of emissions as well as their peak altitudes.

[9] We first examine in Figure 5 how the CO Cameron bands and CO₂⁺ doublet emissions are linked together. We first focus on Figures 5a and 5b, presenting the brightness of CO versus CO₂⁺ and the altitude of the CO versus the CO₂⁺ emission, respectively. It is apparent that the CO and CO₂⁺ brightness are highly correlated, with a linear correlation coefficient *r* of 0.98 and a mean ratio of 4.7 between the two intensities. This result is not unexpected since the CO (a³Π) and CO₂⁺ (B²Σ⁺) states are both mainly produced by processes involving CO₂ as the target molecule [*Barth et al.*, 1971]. Although they are not identical, we also notice that the peak

altitudes covary. Using MARINER 9 data, *Stewart et al.* [1972] found that the ratio between brightness intensities of these emissions was equal to 4.2, which is quite close to the value deduced from the SPICAM observations. Therefore, as these two emissions behave similarly, we will now mainly concentrate on plots for the CO Cameron emission.

[10] The behavior of the CO Cameron intensities was discussed by *Leblanc et al.* [2006]. They presented the variation of the peak intensity versus the solar zenith angle at the tangent point of the line of sight. As these intensities have now been corrected from the CO 4P bands emission, they are shown again in Figure 6a. We find a clear dependence, as the solar flux penetrates less deep into the atmosphere at large zenith angles. This behavior is expected for a Chapman layer [*Hantsch and Bauer*, 1990] with the expression

$$I \propto \sqrt{\cos(SZA)} \quad (1)$$

which describes a clear dependence with the solar zenith angle.

[11] Another aspect of the intensity variations can be described by the F10.7 solar flux index dependence. Since the index is measured from Earth, we first adapted the values to account for the angle formed by Earth, Sun and Mars. Figure 7 shows the observed peak intensity versus the F10.7 index corrected for the seasonal variation of the Sun-Mars distance. The data set is split into three sets of solar zenith angle ranging from 0° to 35° (red curve), 35° to 55° (green curve) and 55° to 90° (blue curve). The plots show only a weak relationship between peak intensities and solar activity. We also note that the trend is globally the same for different ranges of solar zenith angles. If we further examine the relationship between the brightness intensities and the F10.7

Table 3. CO₂⁺ Production Reactions for CO₂⁺ Doublet Emission and References for Cross Sections and Rate Coefficients^a

| Process | Reactions | References |
|----------------|--|-----------------------------|
| 5 ^b | $\text{CO}_2 + h\nu \rightarrow (\text{CO}_2^+)^* + e^-$ | <i>Padiál et al.</i> [1981] |
| 6 | $\text{CO}_2 + e^- \rightarrow (\text{CO}_2^+)^* + 2e^-$ | <i>Itikawa</i> [2002] |

^aThe photoionization and photoabsorption cross-section data and branching ratios for CO₂, CO, O, and N₂ were taken from the Photo Cross Sections and Rate Coefficients database by W. Huebner and R. Link (<http://amop.space.swri.edu/>) [*Huebner et al.*, 1992].

^bThe cross section for this process was calculated as the total CO₂ photoionization cross section multiplied by the branching ratio taken from *Padiál et al.* [1981].

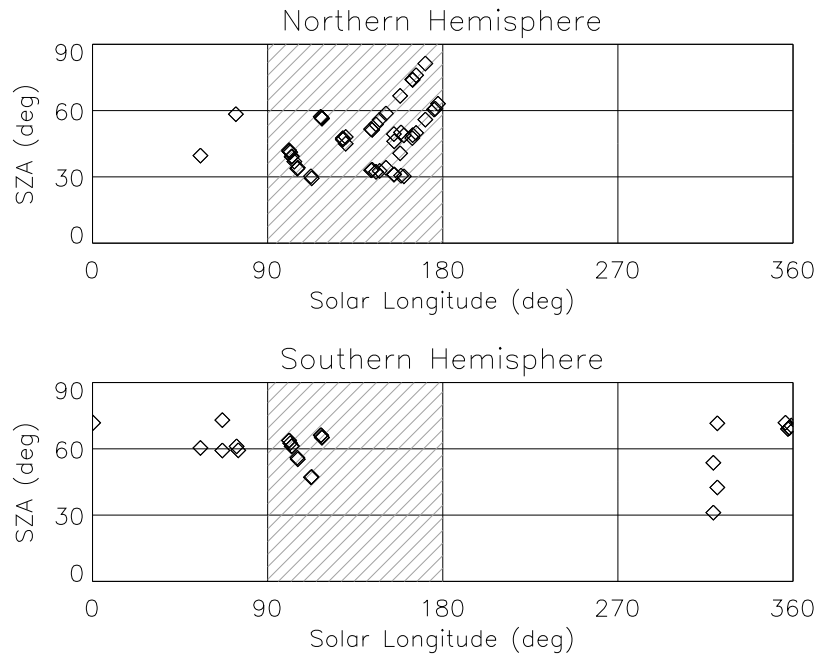


Figure 2. Solar zenith angle coverage of the airglow observations across the different seasons (represented by solar longitude). (top) Northern Hemisphere and (bottom) Southern Hemisphere. The filled area represents the season on which our analysis is focused.

index for low solar zenith angles, the following linear expression is obtained:

$$I_{limb} = 0.82 F_{10.7} + 74.9 \quad (2)$$

where I_{limb} is the peak brightness intensity recorded in limb mode and expressed in kilorayleighs (kR). During the Mariner 9 mission, *Stewart et al.* [1972] derived a similar formula for the subsolar point in the Martian atmosphere:

$$I_{zen} = 0.0620 F_{10.7} + 4.588 \quad (3)$$

where I_{zen} is the zenith brightness intensity expressed in kR. If we assume that the local emission rate of CO Cameron can be approximately modeled by a Chapman function:

$$I(z) = I_m \exp\left(1 - \frac{z - z_m}{H} - \exp\left(-\frac{z - z_m}{H}\right)\right) \quad (4)$$

where I_m , z_m and H are the peak emission rate (in kR/km), the peak altitude (in km) and the topside scale height, respectively, of the CO Cameron emission (the exponentially decreasing rate of the profile topside), and $I(z)$ is the emission rate at the z altitude (also in kR/km), the relations between I_{zen} , I_{limb} , and I_m may be written:

$$I_{zen} = \int_0^{\infty} I(z) dz = (H I_m e) \times (1 - \exp(-\exp(z_m/H))) \approx H I_m e \quad (5)$$

and

$$I_{limb} = \begin{cases} 23.2 I_{zen} & \text{for } H = 14.0 \text{ km} \quad (\text{SPICAM observations}) \\ 20.5 I_{zen} & \text{for } H = 17.8 \text{ km} \quad (\text{MARINER 9 observations}) \end{cases} \quad (6)$$

The relations (6) have been deduced numerically by integrating (4) along a line of sight. They do not depend on z_m if it is kept in a reasonable range ($z_{average} \pm 30$ km). Using (6), we can thus reformulate expression (2) as

$$I_{zen} = 0.034 F_{10.7} + 3.125 \quad (7)$$

which is within a factor of 2 of the relation found with MARINER 9. We note that the season during which the

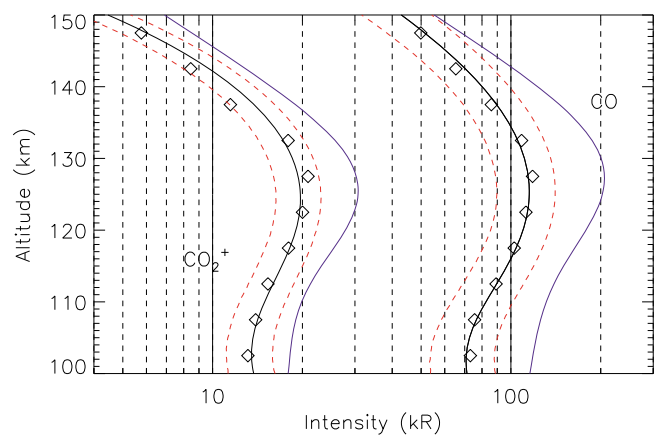


Figure 3. Typical limb profiles of airglow emissions observed during orbit 1267 (Lat = 54°N, SZA = 52°, and Ls = 143°). The observed CO Cameron and CO₂⁺ doublet limb brightness have been binned into 5 km cells and are represented by black diamonds. Red dashed curves correspond to the respective profiles plus or minus 1 standard deviation. The blue curves were calculated with the dayglow model for the same observational conditions as the observations.

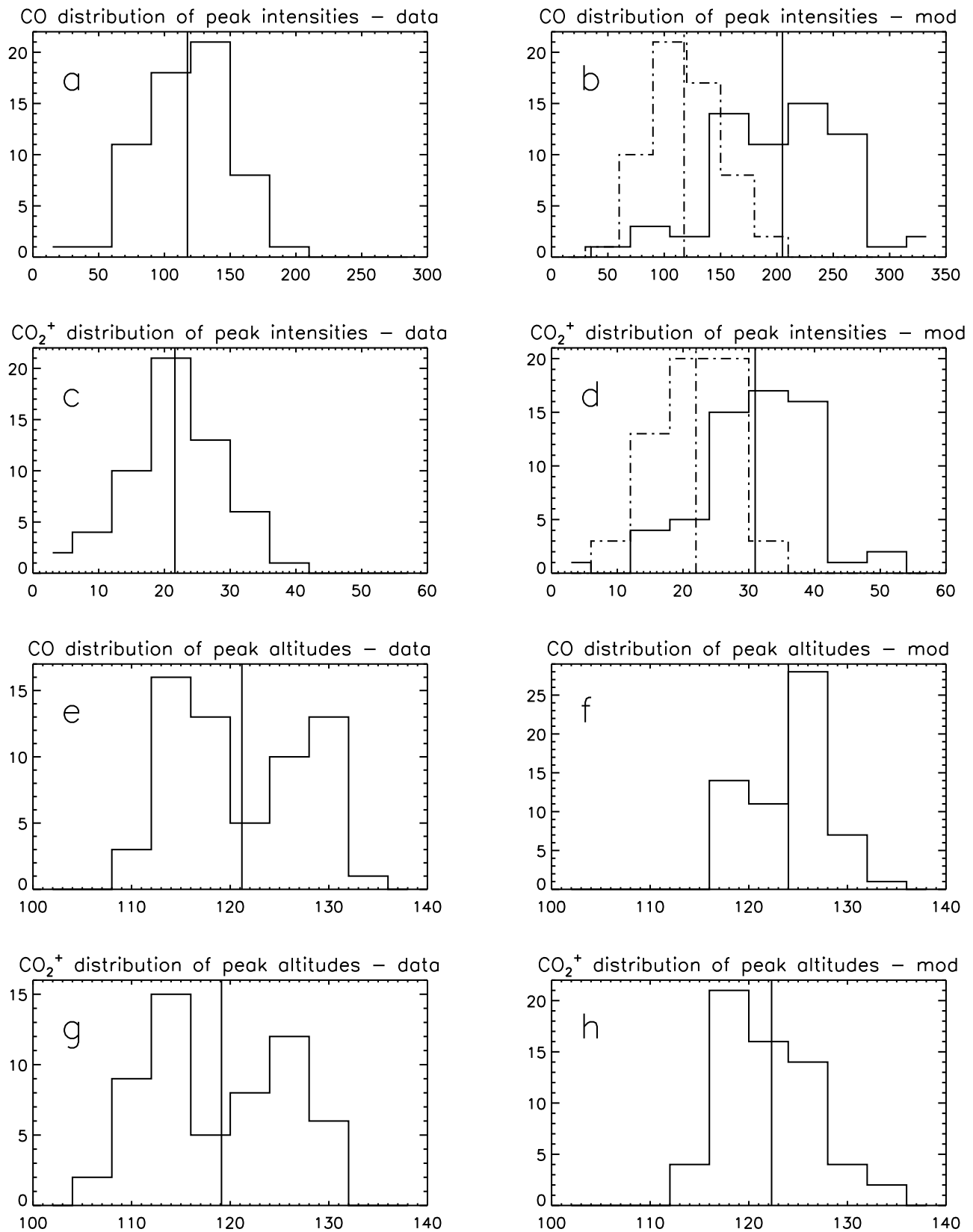


Figure 4. Data distribution histograms. (a) CO peak brightness (data). (b) CO peak brightness (model). The dot-dashed line refers to the scaled brightness (see text). (c) CO₂⁺ peak brightness (data). (d) CO₂⁺ peak brightness (model). The dot-dashed line refers to the scaled brightness (see text). (e) CO peak altitude (data). (f) CO peak altitude (model). (g) CO₂⁺ peak altitude (data). (h) CO₂⁺ peak altitude (model). The vertical lines indicate the mean values.

Table 4. Distribution Characteristics of Observations and Modeling^a

| | CO Cameron | | CO ₂ ⁺ Doublet | |
|--------------|-----------------------------|----------------------------|--------------------------------------|----------------------------|
| | Average Peak Intensity (kR) | Average Peak Altitude (km) | Average Peak Intensity (kR) | Average Peak Altitude (km) |
| Observations | 118 ± 33 | 121.1 ± 6.5 | 21.6 ± 7.2 | 119.1 ± 7.0 |
| Model | 205 ± 59 | 124.1 ± 3.9 | 31.0 ± 8.5 | 122.3 ± 4.3 |

^aThe uncertainties listed for the observations and model correspond to 1 standard deviation.

observations were made with SPICAM and MARINER 9 are different. MARINER 9 observed the airglow near $L_s = 312^\circ$ whereas SPICAM collected observations for L_s ranging from 90° to 180° (for our selected data set) with a mean L_s of 134.6° . This difference of solar longitudes (for a given F10.7 index) generates a variation of solar flux due to the changing Sun-Mars distance given by

$$\alpha = \left(\frac{1 + e \cos(L_{S_{SPI}} - 90)}{1 + e \cos(L_{S_{MAR}} - 90)} \right)^2 \quad (8)$$

$L_{S_{SPI}}$ and $L_{S_{MAR}}$ are the mean solar longitudes where SPICAM and MARINER 9 observations, respectively, have been performed; α is the ratio of the derived solar flux incident to the Martian atmosphere and e is the orbit eccentricity of Mars. Using values of $L_{S_{SPI}} = 134.6^\circ$ and $L_{S_{MAR}} = 312^\circ$, we

find $\alpha = 1.31$, and we derive the formula for I_{zen} adapted to the Mariner 9 conditions:

$$I_{zen} = 0.044 F_{10.7} + 4.093 \quad (9)$$

Comparing with expression (3), we deduce that these intensities are within a mean factor of 1.27 of those derived by *Stewart et al.* [1972]. This result largely reduces the discrepancies pointed out by *Leblanc et al.* [2006].

[12] We now focus on the peak altitudes of the two emissions. Figure 8a shows the peak altitude as a function of the season (represented by the solar longitude L_s). A very clear trend is apparent, showing higher peak altitudes as solar longitude increases. The change in peak altitudes of the CO Cameron profiles clearly reflects a change in the CO₂ density at the altitude where emissions appear. The mean local times

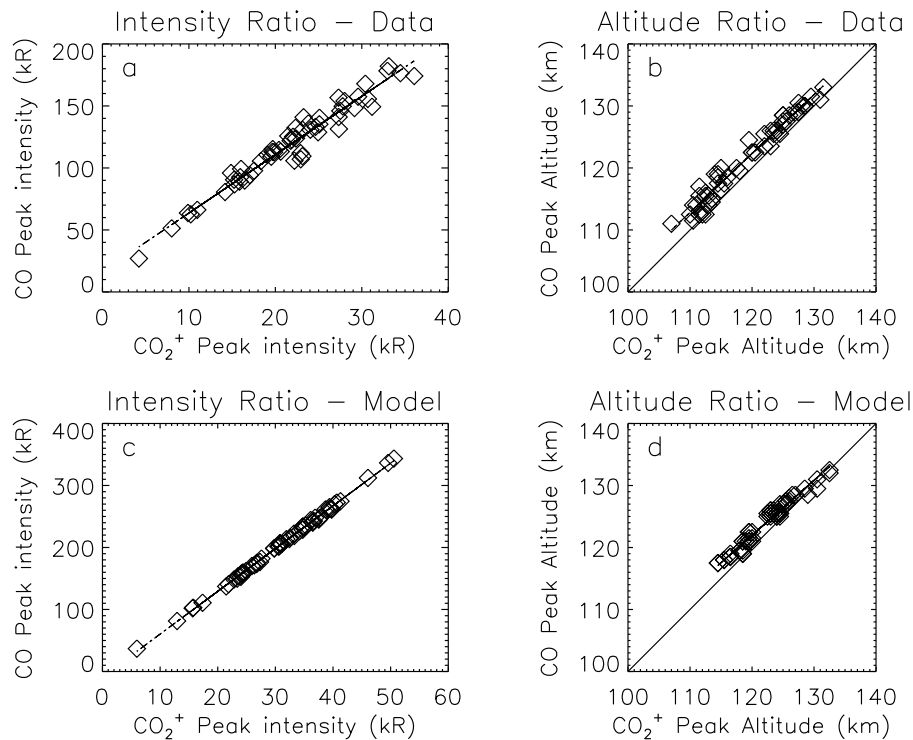


Figure 5. (a) Ratio between the observed CO and CO₂⁺ maximum brightness as observed at the tangent point along the line of sight. The linear regression ratio is equal to 4.7, and the correlation coefficient is 0.98. (b) Ratio between the observed CO and CO₂⁺ altitudes corresponding to the maximum brightness as observed at the tangent point along the line of sight. The mean difference of altitude is equal to 2.4 km, and the linear correlation coefficient is 0.98. (c) Ratio between modeled CO and CO₂⁺ maximum brightness as calculated at the tangent point along the line of sight. The mean ratio is equal to 0.15, and the linear regression coefficient is 1.00. (d) Ratio between modeled CO and CO₂⁺ altitudes corresponding to the maximum brightness as calculated at the tangent point along the line of sight. The difference of altitude is equal to 1.7 km, and the regression coefficient is 0.98.

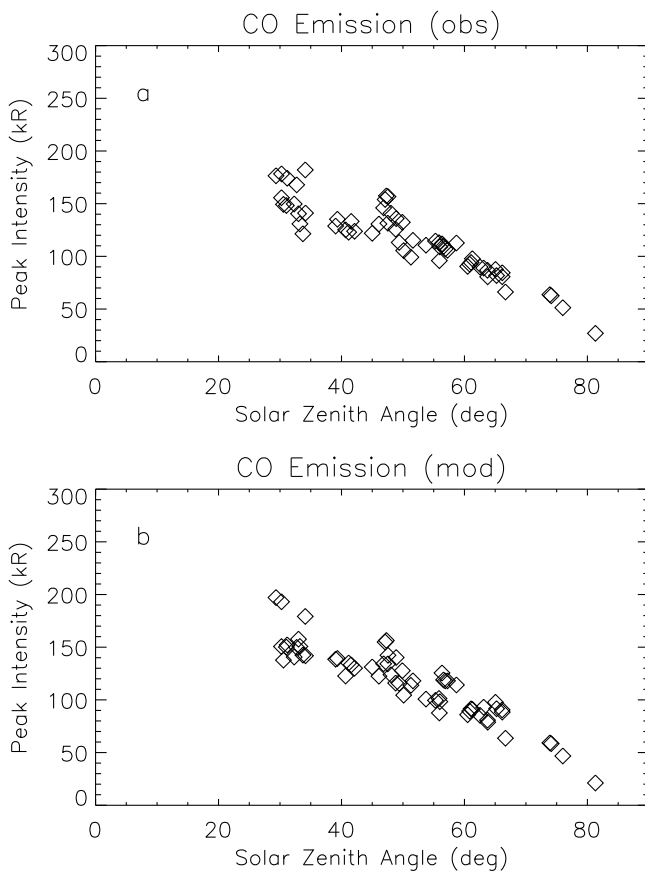


Figure 6. Variation of CO Cameron bands peak brightness as a function of solar zenith angle. Each observation is represented by a diamond. (a) Observed values. (b) Modeled values. The trends in both Figures 6a and 6b are clearly noticeable with correlation coefficients close to unity.

corresponding to the Ls values in the ranges 90° – 135° and 135° – 180° are quite close with 1506 LT for the first range and 1411 LT for the second one, whereas mean latitudes are 3.9° and 50.9° , respectively. As it was discussed by *Hantsch and Bauer* [1990], a dependence of the peak altitudes with the solar zenith angle is expected. Therefore, we need to discriminate between a latitudinal and a season effect for this increase of the peak altitude. A recent work of *Forget et al.* [2009] demonstrated that the CO_2 density at 130 km is directly dependent on the amount of dust contained into the Mars atmosphere. The CO_2 density was increased by a large factor from Ls = 90° to Ls = 180° , for all domains of latitudes or local times. We have also investigated a possible effect of solar zenith angle on the peak altitude and we found that for a restricted range of solar zenith angles from 45° to 60° , the increase of the peak altitude as a function of the solar longitude was still reproduced. These points are shown in red in Figure 8a. With the help of the model described further in the text, we found that the calculated increase of peak altitude for a fixed neutral atmospheric model is only 3.5 km when the solar zenith angle varies from 45° to 60° . This clearly argues that the main factor controlling the altitude of the emission layer is the CO_2 density profile that may exhibit major changes with the season considered. Therefore, Figure 8a mostly reflects the variation in local CO_2 density

and demonstrates that the CO Cameron (or CO_2^+ doublet) airglow can be a very good indicator of density changes in its region of emission.

3. Comparison With Model Calculations

[13] The airglow model used for comparison with the observations was described by *Shematovich et al.* [2008] and simulates airglow emissions on Mars and Venus [*Gérard et al.*, 2008b]. The photoelectron energy spectrum is based on an approach using the Direct Simulation Monte Carlo method where energy degradation directly integrates physical processes. In the Martian atmosphere, photoelectrons are mainly produced by photoionization of CO_2 , N_2 , CO and O. They lose their energy by collisions with the ambient gas. In ionization collisions, newly energetic electrons are created and can play a similar role. Their pitch angle and energy are calculated using an integral form of the formula of *Green and Sawada* [1972], and appropriate cross sections for the different impacted species. Following elastic collisions, new pitch angles are directly assigned to photoelectrons using expressions described by *Porter and Jump* [1978] and *Porter*

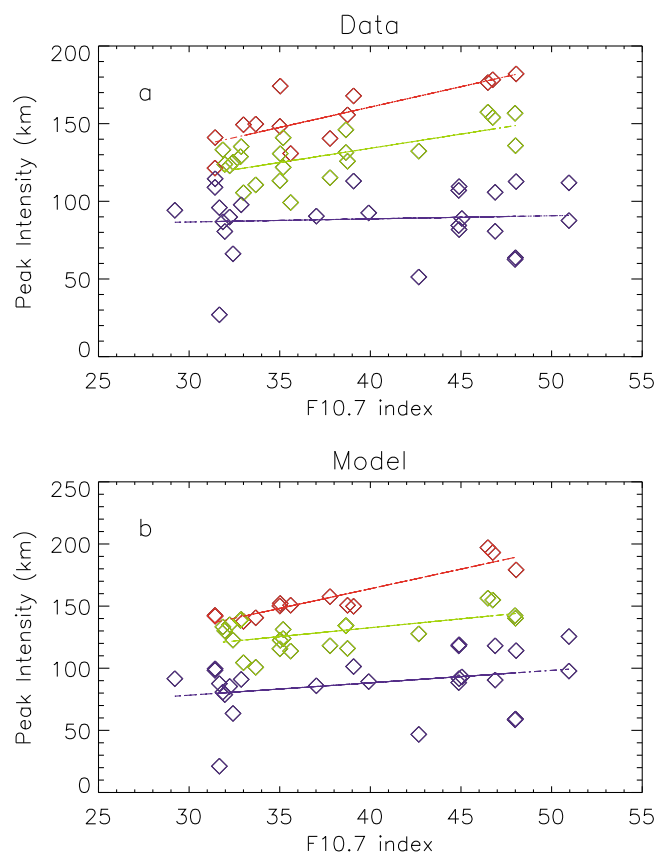


Figure 7. Variation of CO Cameron bands peak brightness as a function of the F10.7 cm solar flux estimated at Mars distance. Each observation is represented by a diamond. Red, green, and blue curves correspond to solar zenith angles ranging from 0° to 35° , from 35° to 55° , and from 55° to 90° , respectively. (a) Observed values. (b) Modeled values. The trends in both Figures 7a and 7b are clearly noticeable although they are more significant in Figure 7b.

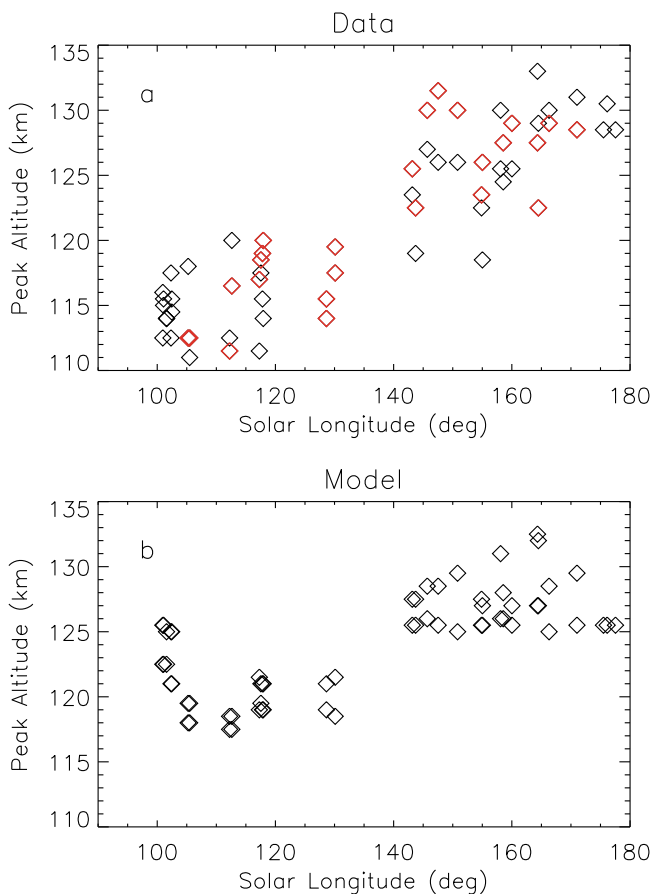


Figure 8. Variation of CO Cameron bands peak altitude as a function of solar longitude. Each observation is represented by a diamond. (a) Observed values; the red points represent data for solar zenith angle ranging from 45° to 60°. (b) Modeled values.

et al. [1987] for angular scattering of electrons. Finally, inelastic collisions are treated using forward scattering approximation. The kinetics and transport of such electrons are described by the kinetic Boltzmann equation, explaining their loss in excess kinetic energy in collision with the ambient gas:

$$\vec{v} \frac{\partial}{\partial \vec{r}} f_e + \vec{s} \frac{\partial}{\partial \vec{v}} f_e = Q_{e,photo}(\vec{v}) + Q_{e,secondary}(\vec{v}) + \sum_{M=O,CO,N_2,CO_2} J(f_e, f_M)$$

where $f_e(\vec{r}, \vec{v})$ and $f_M(\vec{r}, \vec{v})$ are the velocity distribution functions for electrons and for species, respectively, of the ambient gas. The left member of this equation accounts for the transport of electrons inside the Martian gravitational field s . $Q_{e,photo}$ and $Q_{e,secondary}$ are the production rate of primary and of secondary electrons, respectively. J is the elastic and inelastic scattering term for electron collisions with atmospheric species. Details about the method can be found in the earlier work by *Shematovich et al.* [1994, 2008], *Bisikalo et al.* [1995], and *Gérard et al.* [2000]. In order to avoid boundary effects, the limits of the model have been fixed to altitudes of 75 km and 250 km.

[14] Input parameters of the model are the local solar zenith angle, the neutral density profiles determined by latitude, local time and season (described by the solar longitude parameter) and the detailed solar flux. The neutral densities are extracted from the Mars Thermospheric General Circulation Model (MTGCM) of *Bougher et al.* [2006, 2009]. More precisely, neutral species profiles are chosen from a set of 48 MTGCM outputs in such a way that the corresponding parameters are as close as possible to the parameters of the observations. The input fluxes are obtained using SOLAR2000 v2.27 empirical model which provides, for a given date, solar intensities in a wavelength domain ranging from 1.86 nm to 105 nm [*Tobiska, 2004*].

[15] Figure 9 illustrates the different processes calculated by the model as a function of altitude for the simulation of observation retrieved from orbit 1267. Figures 9a and 9b show the processes producing the CO Cameron emission and the CO₂⁺ doublet, respectively. For the CO Cameron emission, we note that the process 2 (electron impact dissociation of CO₂) dominates the other sources by more than a factor 2 whereas it is the process 5 (photoionization of CO₂) that is mainly involved in the CO₂⁺ doublet emission. This result was already reported by *Leblanc et al.* [2006] and *Simon et al.* [2009], who discussed the different processes leading to airglow emission. The emission rates caused by each process in the other observations have been analyzed

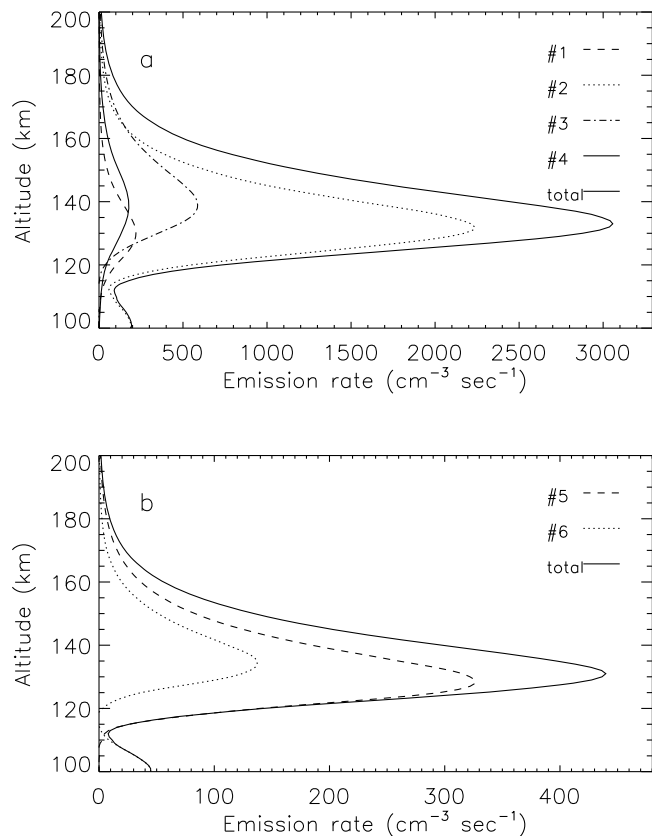


Figure 9. (a) Emission rates as a function of altitude for the CO Cameron emission. The different processes are listed in Table 2. (b) Emission rates as a function of altitude for the CO₂⁺ doublet emission. The different processes are listed in Table 3.

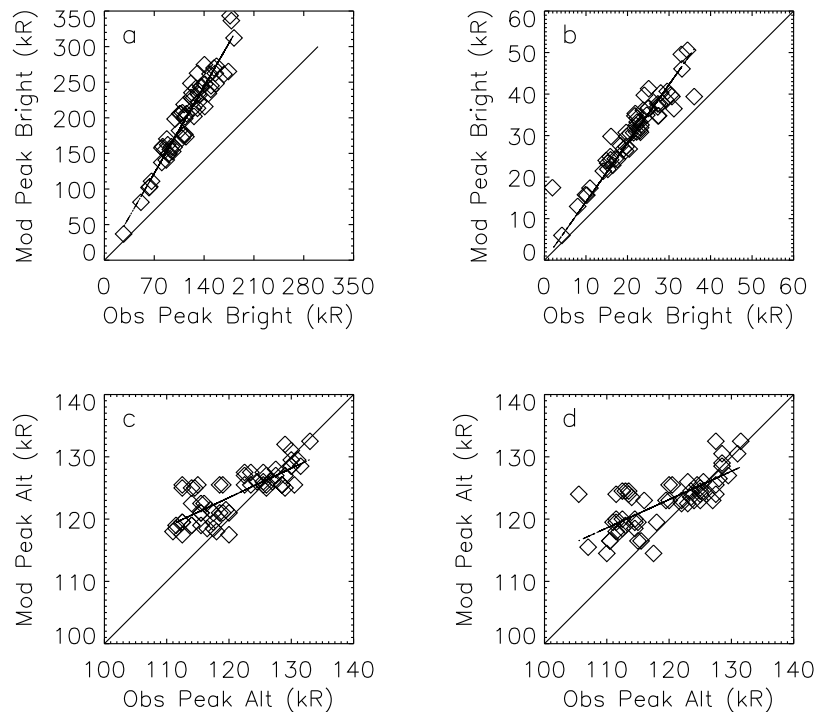


Figure 10. (a) Ratio between modeled and observed CO Cameron bands peak brightness. The mean intensity ratio is equal to 1.74, which implies that our model systematically overestimates the brightness of the CO Cameron emission (see text). (b) Ratio between modeled and observed CO₂⁺ doublet peak brightness. The mean intensity ratio is equal to 1.41 (see text). (c) Modeled CO Cameron peak altitudes versus the observed values. (d) Modeled CO₂⁺ doublet peak altitudes versus the observed values.

and tend to show the same relative importance as in Figures 9a and 9b.

[16] In order to investigate the observed variability, we simulated each observed profile of CO Cameron and CO₂⁺ doublet with the model. Therefore, the code was run for the conditions corresponding to each of the 33 individual limb profiles. The volume emission rates of the CO Cameron and CO₂⁺ bands were calculated and integrated along the line of sight to simulate the observed limb profiles. The altitude of the airglow maximum and the corresponding peak value was then obtained for comparison with the observations.

[17] In Figure 10, we have plotted the intensity of CO and CO₂⁺ peak brightness obtained from the observations versus the CO and CO₂⁺ modeled ones. It is apparent that our model overestimates the CO Cameron intensity on the average by about 74% and the CO₂⁺ doublet by 41%. These differences can be a consequence of different factors: (1) a general bias in the SOLAR2000 intensities used as inputs to our model, (2) a problem of calibration or noise subtraction, and (3) uncertainties in the cross sections in the airglow code. The first source can be excluded since a bias factor has never been reported for SOLAR2000 in the past. In the same way, a calibration or a noise subtraction error can also be eliminated as we know the magnitude of such errors: the uncertainty on the relative calibration [Leblanc *et al.*, 2006] is 15% and errors presented in Figure 3 (taking noise subtraction into account) are smaller than the differences between data and model. As it has been shown previously, such a difference cannot be produced by an inadequate CO₂ profile as it principally acts on the altitude of the emission peak and not on the

airglow maximum intensities. The electron impact cross section for the excitation of the Cameron system proposed by Itikawa [2002] is known within a factor of 2, as determined from the comparison of earlier studies [Furlong and Newell, 1996; Erdman and Zipf, 1983]. In addition, the photoionization cross section of CO₂ to produce CO₂⁺ in the B state is subject to uncertainties. Indeed, a crossover transition occurs between the A and B states of the CO₂⁺ ion, resulting in a quantum yield for the CO₂⁺ (B²Σ → X²Σ) emission. Johnson *et al.* [1984] suggested a branching ratio from the CO₂⁺ B state to the A state of 0.42 ± 0.07. Application of this branching ratio would reduce our discrepancy to a factor of 1.04 instead of 1.41, in excellent agreement with the observations. In this study, we use the ionization cross section calculated by Padial *et al.* [1981] with a quantum yield of 100%, until a more detailed analysis of this question has been carried out. All these uncertainties can be a source of discrepancy between the SPICAM data and our airglow modeling. In a similar way, Simon *et al.* [2009] had to reduce their calculated intensities to match the observed brightness. They also attributed this difference to the cross section uncertainties. In order to compare more easily the observations with the model results, and emphasize the observed variability rather than the absolute intensities, we have empirically divided all modeled intensities in Figures 6b and 7b by the corresponding correction factors. Moreover, one can note that some discrepancies appear between our calculated airglows intensities and those presented by Shematovich *et al.* [2008]. This difference can be caused by different factors: (1) the Monte Carlo code has been updated with most recent collision cross

sections and intrinsic parameters, and, therefore, the code version is not identical to the one of *Shematovich et al.* [2008]; (2) our airglow brightness is corrected for underlying emissions and may thus be weaker, increasing the difference pointed out with the model; (3) the way the input solar fluxes are obtained for a given date may be different; and, finally, (4) the input neutral atmosphere is provided by an updated version of the MTGCM model.

[18] The model results are presented together with the observations in Figures 3–8. In Figure 3, the observed peak altitude values are very well reproduced. The discrepancy in the brightness between the modeled limb profiles (represented in blue) intensity and the data is however apparent. This difference can also be noticed in the distribution function presented in Figures 4b and 4d. Concerning the variability of the peak brightness, both distribution histograms of CO Cameron and CO₂⁺ doublet are fairly well reproduced by the airglow model coupled with MTGCM neutral density outputs. Nonetheless, the modeled peak altitude distributions differ from the data distributions. This difference will be analyzed further below. In Figure 5c, it is seen that the linear proportionality between the CO₂⁺ doublet and the CO Cameron emissions brightness is well reproduced. Similarly, in Figure 5d, the altitude difference between the two airglow layers is also simulated. This suggests the different processes coming into play in the airglow formation and calculated by the model are well estimated. In Figure 6b, we note that the variation of the peak intensities with respect to solar zenith angle is also fairly well reproduced. The model is thus able to efficiently simulate the variations with solar zenith angle and the drop of intensity observed in regions further away from the subsolar point. Figure 7b illustrates the simulated dependence on solar activity as defined by the F10.7 solar flux index used as a proxy of solar EUV flux for Mars. The correlation observed between the peak intensities and the F10.7 index is predicted by the model. Since processes 1, 4 and 6 are directly controlled by the incoming solar flux, this correlation in our model was expected and is a response to the changing amount of ionizing solar flux.

[19] We directly note in Figure 8b that the general increase of the peak altitude is also simulated by the model. However, the peak altitudes for Ls ranging from 90° to 135° are overestimated by 5 km. We have shown that the altitude of the airglow peak reflects the CO₂ density profile; we conclude that this discrepancy stems from differences between the actual CO₂ columns and the profile used in the model. Note also that the region of discrepancy includes equatorial latitudes whereas the right portion of Figure 8b contains data collected for a mean latitude of 50.9°N. As was demonstrated by *Forget et al.* [2009], the increase in CO₂ density at 130 km was very sharp during this season and these variations can hardly be reproduced by averaged GCM simulations [*Forget et al.*, 2009, Figure 11]. Furthermore, simulations for the same MEX/SPICAM sampling period (Ls = 90 to 135) by *McDunn et al.* [2010] using the Mars Thermospheric General Circulation Model (MTGCM) show overpredicted CO₂ densities at 130 km [see *McDunn et al.*, 2010, Figure 7], regardless of the empirical horizontal dust distribution prescribed. This feature is similar to that of *Forget et al.* [2009]. Improper vertical dust distributions may be responsible for these discrepancies in both models. As a result, overestimated

dayglow peak altitudes are simulated in this study for Ls = 90 to 135. However, we note in the histograms presented in Figure 4 and in Table 4 that the mean values of peak altitudes are well estimated within 2–3 km, which is approximately equal to the model vertical resolution.

4. Conclusion

[20] The CO Cameron and CO₂⁺ doublet emissions in the Martian atmosphere are highly variable. Restricting our study to one specific season (Ls = 90° to 180°), we have found that the distribution of peak brightness is very widespread, with a standard deviation of about 30%. The altitudes of the peak emission vary in a 25 km range for both emissions, with a standard deviation of 7 km. We have shown that this variability is controlled by several parameters. The solar zenith angle directly influences the brightness intensity. Solar activity represented by the F10.7 index also controls the intensity of both emissions to some extent. We have also shown that the relationship we derived between the F10.7 index and the peak brightness of limb profiles is in good agreement with the previous results deduced with MARINER 9 observations by *Stewart et al.* [1972]. Moreover, the altitude of the emission peaks is shown to increase between Ls = 90 and Ls = 180. We interpret the increase as a consequence of the changing CO₂ profile which introduces a seasonal dependence, especially during this particular year of observation. Consequently, the dayglows analyzed in this paper can be suitable tracers for the monitoring of the CO₂ density on the dayside of the planet.

[21] Each individual profile has been compared with the result of a model calculation based on the airglow code developed by *Shematovich et al.* [2008]. We find that our calculations overestimate the CO brightness intensity by a factor of 1.74 and the CO₂⁺ emission intensity by a factor of 1.41. However, these factors remain constant as the solar zenith angle or the F10.7 index change, implying that the model is able to efficiently reproduce the brightness variation within these parameters, and indicating that they are the physical sources of the brightness variability. These discrepancies may stem from uncertainties on the electron impact cross section of CO (a³Π) which is only known within a factor of 2. Similarly the excitation cross section of CO₂ into the CO₂⁺ (B²Σ → X²Σ) state is subject to discussion, which provides a possible explanation for the overestimate of the CO₂ doublet intensity. We also note that the model was unable to correctly simulate the mean observed altitude peak value for Ls values ranging from 90° to 135°. Since the altitude of the airglow layer is principally controlled by the CO₂ density profile at the location of the airglow emission, it is expected that more realistic CO₂ profiles will enable the airglow code to better reproduce the observed altitude variability. Improvements in the prescription of vertical dust distributions in GCMs may also be required.

[22] **Acknowledgments.** The authors thank the SPICAM and the MEX teams. J.-C. Gérard is supported by the Belgian Fund for Scientific Research. S. W. Bougher is supported by the NASA Mars Data Analysis Program (grant NNX07A084G). This work was funded by the PRODEX program of the European Space Agency managed with the help of the Belgian Space Policy Office and by IISN grant 4.4508.06.

References

- Anderson, D. E., Jr., and C. W. Hord (1971), Mariner 6 and 7 ultraviolet spectrometer experiment: Analysis of hydrogen Lyman-alpha data, *J. Geophys. Res.*, **76**, 6666–6673, doi:10.1029/JA076i028p06666.
- Barth, C. A., C. W. Hord, J. B. Pearce, K. K. Kelly, G. P. Anderson, and A. I. Stewart (1971), Mariner 6 and 7 ultraviolet spectrometer experiment: Upper atmosphere data, *J. Geophys. Res.*, **76**, 2213–2227, doi:10.1029/JA076i010p02213.
- Barth, C. A., A. I. Stewart, C. W. Hord, and A. L. Lane (1972), Mariner 9 ultraviolet spectrometer experiment: Mars airglow spectroscopy and variations in Lyman alpha, *Icarus*, **17**, 457–462, doi:10.1016/0019-1035(72)90011-5.
- Bertaux, J.-L., et al. (2006), SPICAM on Mars Express: Observing modes and overview of UV spectrometer data and scientific results, *J. Geophys. Res.*, **111**, E10S90, doi:10.1029/2006JE002690.
- Bisikalo, D. V., V. I. Shematovich, and J.-C. Gérard (1995), A kinetic model of the formation of the hot oxygen geocorona: 2. Influence of O⁺ ion precipitation, *J. Geophys. Res.*, **100**, 3715–3720, doi:10.1029/94JA03196.
- Bougher, S. W., J. M. Bell, J. R. Murphy, M. A. Lopez-Valverde, and P. G. Withers (2006), Polar warming in the Mars thermosphere: Seasonal variations owing to changing insolation and dust distributions, *Geophys. Res. Lett.*, **33**, L02203, doi:10.1029/2005GL024059.
- Bougher, S. W., T. M. McDunn, K. A. Zoldak, and J. M. Forbes (2009), Solar cycle variability of Mars dayside exospheric temperatures: Model evaluation of underlying thermal balances, *Geophys. Res. Lett.*, **36**, L05201, doi:10.1029/2008GL036376.
- Conway, R. R. (1981), Spectroscopy of the Cameron bands in the Mars airglow, *J. Geophys. Res.*, **86**, 4767–4775, doi:10.1029/JA086iA06p04767.
- Cox, C., A. Saglam, J.-C. Gérard, J.-L. Bertaux, F. González-Galindo, F. Leblanc, and A. Reberac (2008), Distribution of the ultraviolet nitric oxide Martian night airglow: Observations from Mars Express and comparisons with a one-dimensional model, *J. Geophys. Res.*, **113**, E08012, doi:10.1029/2007JE003037.
- Erdman, P. W., and E. C. Zipf (1983), Electron-impact excitation of the Cameron system ($a^3\pi \rightarrow X^1\Sigma$) of CO, *Planet. Space Sci.*, **31**, 317–321, doi:10.1016/0032-0633(83)90082-X.
- Feldman, P. D., E. B. Burgh, S. T. Durrance, and A. F. Davidsen (2000), Far-ultraviolet spectroscopy of Venus and Mars at 4A resolution with the Hopkins Ultraviolet Telescope on Astro-2, *Astrophys. J.*, **538**, 395–400, doi:10.1086/309125.
- Forget, F., F. Montmessin, J.-L. Bertaux, F. González-Galindo, S. Lebonnois, E. Quémerais, A. Reberac, E. Dimarellis, and M. A. López-Valverde (2009), Density and temperatures of the upper Martian atmosphere measured by stellar occultations with Mars Express SPICAM, *J. Geophys. Res.*, **114**, E01004, doi:10.1029/2008JE003086.
- Fox, J. L. (2004), CO₂ dissociative recombination: A source of thermal and nonthermal C on Mars, *J. Geophys. Res.*, **109**, A08306, doi:10.1029/2004JA010514.
- Fox, J. L., and A. Dalgarno (1979), Ionization, luminosity, and heating of the upper atmosphere of Mars, *J. Geophys. Res.*, **84**, 7315–7333, doi:10.1029/JA084iA12p07315.
- Furlong, J. M., and W. R. Newell (1996), Total cross section measurement for the metastable $a^3\Pi$ state in CO, *J. Phys. B At. Mol. Opt. Phys.*, **29**, 331–338, doi:10.1088/0953-4075/29/2/020.
- Gérard, J.-C., B. Hubert, D. V. Bisikalo, and V. I. Shematovich (2000), A model of the Lyman- α line profile in the proton aurora, *J. Geophys. Res.*, **105**, 15,795–15,805, doi:10.1029/1999JA002002.
- Gérard, J.-C., C. Cox, A. Saglam, J.-L. Bertaux, E. Villard, and C. Nehmé (2008a), Limb observations of the ultraviolet nitric oxide nightglow with SPICAV on board Venus Express, *J. Geophys. Res.*, **113**, E00B03, doi:10.1029/2008JE003078.
- Gérard, J.-C., B. Hubert, V. I. Shematovich, D. V. Bisikalo, and G. R. Gladstone (2008b), The Venus ultraviolet oxygen dayglow and aurora: Model comparison with observations, *Planet. Space Sci.*, **56**, 542–552, doi:10.1016/j.pss.2007.11.008.
- Green, A. E. S., and T. Sawada (1972), Ionization cross sections and secondary electron distributions, *J. Atmos. Terr. Phys.*, **34**, 1719–1728, doi:10.1016/0021-9169(72)90031-1.
- Gutcheck, R. A., and E. C. Zipf (1973), Excitation of the CO fourth positive system by the dissociative recombination of CO₂⁺ ions, *J. Geophys. Res.*, **78**, 5429–5436, doi:10.1029/JA078i025p05429.
- Hanson, W. B., S. Sanatani, and D. R. Zuccaro (1977), The Martian ionosphere as observed by the Viking retarding potential analyzers, *J. Geophys. Res.*, **82**, 4351–4363, doi:10.1029/JS082i028p04351.
- Hantsch, M. H., and S. J. Bauer (1990), Solar control of the Mars ionosphere, *Planet. Space Sci.*, **38**, 539–542, doi:10.1016/0032-0633(90)90146-H.
- Huebner, W. F., J. J. Keady, and S. P. Lyon (1992), Solar photo rates for planetary atmospheres and atmospheric pollutants, *Astrophys. Space Sci.*, **195**, 1–294, doi:10.1007/BF00644558.
- Itikawa, Y. (2002), Cross sections for electron collisions with carbon dioxide, *J. Phys. Chem. Ref. Data*, **31**(3), 749–767, doi:10.1063/1.1481879.
- Johnson, M. A., R. N. Zare, J. Rostas, and S. Leach (1984), Resolution of the A/B photoionization branching ratio paradox for the ¹²CO₂⁺ B(000) state, *J. Chem. Phys.*, **80**, 2407–2428, doi:10.1063/1.446991.
- Lawrence, G. M. (1972), Photodissociation of CO₂ to produce CO($a^3\Pi$), *J. Chem. Phys.*, **56**, 3435–3442, doi:10.1063/1.1677717.
- Leblanc, F., J. Y. Chaufray, J. Lilensten, O. Witasse, and J.-L. Bertaux (2006), Martian dayglow as seen by the SPICAM UV spectrograph on Mars Express, *J. Geophys. Res.*, **111**, E09S11, doi:10.1029/2005JE002664.
- McDunn, T. L., S. W. Bougher, J. Murphy, M. D. Smith, F. Forget, J.-L. Bertaux, and F. Montmessin (2010), Simulating the density and thermal structure of the middle atmosphere (~80–130 km) of Mars using the MGCAM-MTGCAM: A comparison with MEX/SPICAM observations, *Icarus*, **206**, 5–17.
- Padial, N., G. Csanak, B. V. McKoy, and P. W. Langhoff (1981), Photoexcitation and ionization in carbon dioxide: Theoretical studies in the separated-channel static-exchange approximation, *Phys. Rev. A*, **23**, 218–235, doi:10.1103/PhysRevA.23.218.
- Porter, H. S., and F. W. Jump (1978), Analytic total and angular elastic electron impact cross sections for planetary atmospheres, *Comput. Sci. Corp. Rep. CSC/TM-6017*, Goddard Space Flight Cent., Greenbelt, Md.
- Porter, H. S., F. Varosi, and H. G. Mayr (1987), Iterative solution of the multistream electron transport equation: 1. Comparison with laboratory beam injection experiments, *J. Geophys. Res.*, **92**, 5933–5959, doi:10.1029/JA092iA06p05933.
- Rosati, R. E., R. Johnsen, and M. F. Golde (2003), Absolute yields of CO ($a^3\Sigma^+$, $d^3\Delta_i$, $e^3\Sigma^-$) + O from the dissociative recombination of CO₂⁺ ions with electrons, *J. Chem. Phys.*, **119**, 11,630–11,635, doi:10.1063/1.1623480.
- Seiersen, K., A. Al-Khalili, O. Heber, M. J. Jensen, I. B. Nielsen, H. B. Pedersen, C. P. Safvan, and L. H. Andersen (2003), Dissociative recombination of the cation and dication of CO₂, *Phys. Rev. A*, **68**(2), 022708, doi:10.1103/PhysRevA.68.022708.
- Shematovich, V. I., D. V. Bisikalo, and J.-C. Gérard (1994), A kinetic model of the formation of the hot oxygen geocorona: 1. Quiet geomagnetic conditions, *J. Geophys. Res.*, **99**, 23,217–23,228, doi:10.1029/94JA01769.
- Shematovich, V. I., D. V. Bisikalo, J.-C. Gérard, C. Cox, S. W. Bougher, and F. Leblanc (2008), Monte Carlo model of electron transport for the calculation of Mars dayglow emissions, *J. Geophys. Res.*, **113**, E02011, doi:10.1029/2007JE002938.
- Shirai, T., T. Tabata, and H. Tawara (2001), Analytic cross sections for electron collisions with CO, CO₂, and H₂O relevant to edge plasma impurities, *At. Data Nucl. Data Tables*, **79**(1), 143–184, doi:10.1006/andn.2001.0866.
- Simon, C., O. Witasse, F. Leblanc, G. Gronoff, and J.-L. Bertaux (2009), Dayglow on Mars: Kinetic modelling with SPICAM UV limb data, *Planet. Space Sci.*, **57**, 1008–1021, doi:10.1016/j.pss.2008.08.012.
- Skrzypkowski, M. P., T. Gougousi, R. Johnsen, and M. F. Golde (1998), Measurements of the absolute yield of CO($a^3\Pi$) + O products in the dissociative recombination of CO₂⁺ ions with electrons, *J. Chem. Phys.*, **108**, 8400–8407, doi:10.1063/1.476267.
- Stewart, A. I. (1972), Mariner 6 and 7 ultraviolet spectrometer experiment: Implications of CO₂⁺, CO and O airglow, *J. Geophys. Res.*, **77**, 54–68, doi:10.1029/JA077i001p00054.
- Stewart, A. I., C. A. Barth, C. W. Hord, and A. L. Lane (1972), Mariner 9 ultraviolet spectrometer experiment: Structure of Mars' upper atmosphere, *Icarus*, **17**, 469–474, doi:10.1016/0019-1035(72)90012-7.
- Strickland, D. J., G. E. Thomas, and P. R. Sparks (1972), Mariner 6 and 7 ultraviolet spectrometer experiment: Analysis of the OI 1304- and 1356-A emissions, *J. Geophys. Res.*, **77**, 4052–4068, doi:10.1029/JA077i022p04052.
- Strickland, D. J., A. I. Stewart, C. A. Barth, C. W. Hord, and A. L. Lane (1973), Mariner 9 ultraviolet spectrometer experiment: Mars atomic oxygen 1304-A emission, *J. Geophys. Res.*, **78**, 4547–4559, doi:10.1029/JA078i022p04547.
- Tobiska, W. K. (2004), SOLAR2000 irradiances for climate change, aeronomy and space system engineering, *Adv. Space Res.*, **34**, 1736–1746, doi:10.1016/j.asr.2003.06.032.

J.-L. Bertaux, LATMOS, Boulevard d'Alembert 11, F-78280 Guyancourt, France.

S. W. Bougher, Department of Atmospheric, Oceanic and Space Sciences, University of Michigan, Ann Arbor, MI 48109, USA.

C. Cox, J.-C. Gérard, and B. Hubert, Laboratoire de Physique Atmosphérique et Planétaire, Université de Liège, B-4000 Liège, Belgium. (cedric.cox@ulg.ac.be)